NUCLEAR EXCITED LOW-TEMPERATURE PLASMAS IN POROUS METALS: NEW ENERGY FRONTIERS

A. LO
GenAlpha Nuclear Technologies LLC
2525 Elm St., Dallas, TX 75226– USA

Experimental and analytical methods are described for assessing Nuclear-excited Low-Temperature Plasmas generated in high surface area porous metal electrodes. Results from a foundational experiment investigating these plasmas suggest applications in which high specific current extraction [A g^{-1}] is desirable. Follow-on efforts that leverage existing test, research, and training reactors will play a vital role in further exploring this new material configuration in radiation environments.

1. Introduction

Nuclear-excited Low-Temperature Plasmas (NLTPs) occur in gaseous media when they absorb ionizing radiation from nuclear reactions at a sufficient power density. Typically, an NLTP system consists of 1) a solid component in which charged particle-producing nuclear reactions occur and 2) a gaseous component that absorbs the charged particles escaping the solid component. To date, only simple and relatively low specific surface area $\bar{A}$ [cm^2 g^{-1}] solid-gas interfaces have been considered for these systems, such as solid parallel plate and coaxial configurations. Where initial NLTP research pursuits beginning in the 1960s considered broad applications to Direct Energy Conversion (DEC)-based [1] nuclear power and Nuclear Pumped Lasers (NPLs) [2], the only practical device that resulted was the ionization chamber-based neutron sensor [3] – a crucial but rather niche use case. NLTP research was essentially abandoned by the 1990s [4, 5].

A recent experiment (to be published) considered a complex NLTP solid-gas interface: an open-cell reticulated metal foam containing the plasma within the electrode structure. The motivation for using this structure was to increase the electrodes' specific surface area $\bar{A}$ [cm^2 g^{-1}] to increase the specific ion current $\bar{I}_i$ [A g^{-1}] extraction – thus electrical power – through it. NLTPs produced in high $\bar{A}$ electrodes could enhance existing devices (i.e., neutron sensors) and dormant technologies, specifically DEC-based nuclear power.

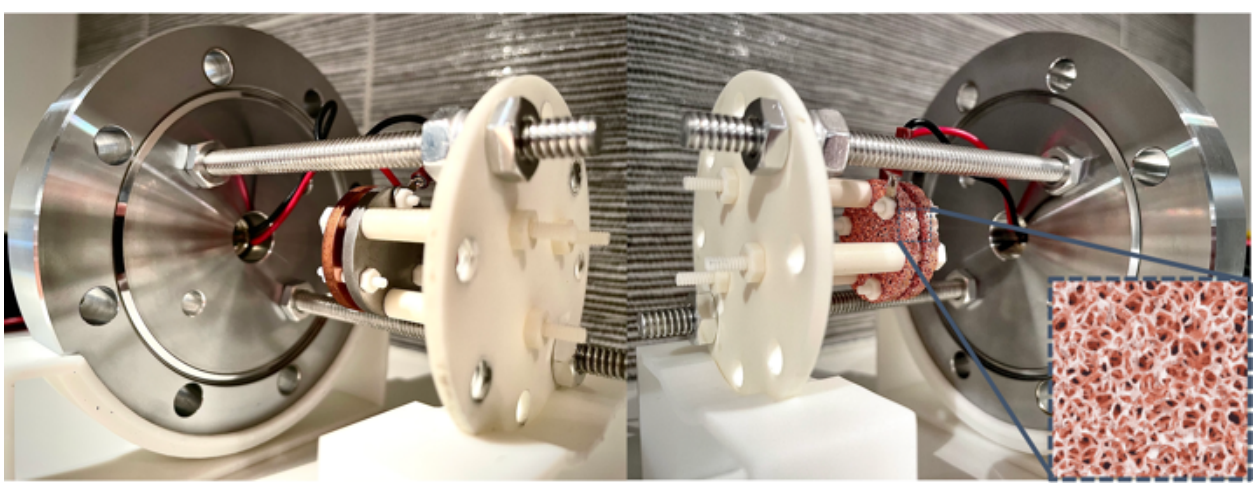

Figure 1: Experimental apparatus for measuring current density extraction from NLTPs using (left) solid and (right) open-cell reticulated copper foam electrodes.

The NLTP was generated by immersing the electrodes in an ionizing radiation field consisting of neutrons (~5x10^{12} n cm^{-2} s^{-1}) and gammas (~2krad hr^{-1}) produced by a Mark II TRIGA reactor at the Nuclear Engineering Teaching Laboratory at the University of Texas at Austin. $\bar{I}_i$ was compared between foam and solid parallel plane electrode devices. The experimental apparatuses are shown in Figure 1.

2. Basic Concepts and Analytical Methods for NLTPs in Two-Component Media

The basic analytical methods used to calculate the energy deposited in a two-component media and resulting plasma parameters are presented in the following sections. The physical quantities of interest can be deduced experimentally or by modeling and simulation (M&S). The former involves current-voltage (I-V) curve measurements in high radiation environments while the latter requires a radiation transport code that can treat high energy (>1keV) charged particle and photon sources.

2.1. Charged Particle Stopping and its Ionization of Gases

High-energy charged particles deposit their energy in gases by ionization and excitation collisions. This energy deposition per unit pathlength dE/dx [eV cm^{-1}] is a complicated function of the particle type, energy, and charge state [6, 7]. For this, computational approaches are usually appropriate for incorporating charged particle transport into physical models. By contrast, the "W" value, a historical term defining the energy cost per ionization collision, assumes a constant value (for a given charged particle and gaseous species) over a wide range of energies [8]; all energies concerning low-energy (<20MeV) nuclear energy sources. $w_{i,a}$ [eV ion^{-1}] to good approximation is 1.71 times the gaseous species' ionization potential $V_{i,a}$ [eV] when the ionizing species is electrons. $w_{i,a}$ and $V_{i,a}$ are listed in Table 1. With knowledge of dE/dx (computationally) and $w_{i,a}$, the number of ionizations per source particle occurring in a gas can be determined.

Table 1. $V_{i,a}$ and $w_{i,a}$ values for high-energy electrons [8].

Gas	He	Ne	Ar	Kr	Xe
$V_{i,a}$ (eV)	24.6	21.6	15.8	14.0	12.1
$w_{i,a}$ (eV)	42.3	36.6	26.4	24.2	22.0

2.2. Energy Deposition in Two-Component Media

The reaction rate density R_{ijl} [cm^{-3} s^{-1}] of streaming particles i into target media j creating reaction type l is

$$R_{ijl} = \phi_{ij}\sigma_{ijl}n_j \tag{2}$$

where ϕ_{ij} [cm^{-2} s^{-1}] is the incident particle flux, σ_{ijl} [cm^2] is the cross section of reaction l between streaming particles i and target media j, and n_j [cm^{-3}] is the particle density of media particles j. The total power density absorbed by the system p_{tot} [W cm^{-3}] is the sum

$$p_{tot} = \sum_{ijkl}\left(R_{ijl}E(E_0)_{l,j\to k}\frac{V_j}{V_k}\right) \tag{3}$$

where $E(E_0)_{l,j\to k}$ [J] is the energy associated with process l originating in media j and depositing in media k, V_j and V_k are the volumes [cm^3] of media j and k, respectively.

Consider the energy deposition of one streaming particle species producing one reaction type in a two-component media, where component 1 is solid and component 2 is gaseous. Assuming $n_2 \ll n_1$ Equation 3 reduces to

$$p_{tot} = p_{solid}[1 + \nu\beta(E_0)] \tag{4}$$

where $p_{solid} = R_{111}E(E_0)_{1,1\to1}$ [W cm^{-3}] is the heat density in the solid component of the media, $\beta(E_0) = E(E_0)_{1,1\to2}/E(E_0)_{1,1\to1}$ is the ratio of the energy deposited in the gaseous and solid components, and $\nu = V_1/V_2$ is the ratio of solid to gaseous volumes. The product $\nu\beta(E_0)$ can be readily calculated using radiation transport codes for arbitrary combinations of material compositions and geometries, reaction types, source particles and energies. Furthermore the product $\nu\beta(E_0)$ (referred to as $\nu\beta$ from here forward) allows the calculation of gaseous power density p_a [W cm^{-3}] via p_{solid} by the definition $p_{tot} \equiv p_{solid} + p_a$. This is a useful formula when considering achievable NLTP parameters given a media's p_{solid} tolerance.

2.3. NLTP parameters n_e and T_e

Two fundamental parameters that characterize plasmas' average behavior are the electron density and temperature, n_e [cm^{-3}] and T_e [K]. To be considered a plasma vice ionized gas, the system's size must be greater than the Debye length λ_D [cm], given by the formula:

$$\lambda_D \sim 6.9\sqrt{\frac{T_e}{n_e}}. \tag{5}$$

In the high-pressure NLTPs under consideration, a spatially uniform bulk density (recombination-dominated profile) and Maxwellian temperature profile for the electrons are assumed as in [9, 10 – Chapter 2]. Then n_e and T_e are solved simultaneously via electron particle and power balance equations, respectively; a complete analysis of these quantities can be found in the author's dissertation [10 – Chapter 3]. The relations for n_e and T_e are

$$n_e^2 = \frac{\nu\beta p_{solid}}{e w_{i,a} k_{dr}(T_e, T_a)} \tag{6}$$

where e [C] is the electron charge and

$$p_{solid} = \frac{e w_{i,a}}{\nu\beta k_{dr}(T_e, T_a)}\left(\frac{n_a \frac{m_e^2}{M} K_{el}(T_e)\left(1 - \frac{T_a}{T_e}\right)}{E_{ave} - kT_e}\right)^2 \tag{7}$$

where $K_{el}(T_e)$ [cm^5 s^{-3}] is the elastic scattering rate constant and $k_{dr}(T_e, T_a) = \alpha_0\left(\frac{T_e}{300}\right)^{-\psi}\left(\frac{T_a}{300}\right)^{-\omega}$ [cm^3 s^{-1}] is molecular ion (dominant ion species) dissociative recombination coefficient. The former's temperature-dependent values are readily obtained by integrating the product $v^3\sigma_{el}$ over a Maxwellian distribution; the latter's values within applicable T_a and T_e are given in Table 2. Equations 4-7 offer a direct and calculable means of establishing the density, temperature, and length scale of an NLTP resulting in gaseous media due to some nuclear heat source p_{solid}.

Table 2. $k_{dr}(T_e, T_a)$ for heavy noble gases for T_a = 300-500K [10 – Chapter 2].

Ion	α_0	ω	ψ	T_e Range (K)
Ne_2^+	1.8x10^{-7}	0.7	0.42	T_e = 300-6300
Ar_2^+	8.1x10^{-7}	0.86	0.64	T_e = 300-10400
Kr_2^+	1.4x10^{-6}	0.97	0.53	T_e = 300-19000
Xe_2^+	8.1x10^{-5}	No data	0.60	T_e = 300-19000

2.4. I-V Characteristic Curves

Characterizing NLTPs via I-V curves has already been considered previously [9, 11]. Those experiments used floating electrode configurations analogous to Figure 1; [9] derived the relation between the ion current I_i and supplied voltage V_s [V],

$$I_i = CA\left(\nu\beta\frac{p_{solid}}{ew_{i,a}}\right)^{3/4} V_s^{1/2} \tag{8}$$

where $C = \left(4x10^{-2}\mu_{a_2^+}\varepsilon_0 e^3\right)^{1/4}$ is a constant value comprised of the ion species mobility, $\mu_{a_2^+}$ [cm^2 V^{-1} s^{-1}] permittivity constant ε_0 [C V^{-1} m^{-1}] and electric charge e [C]. We have replaced the term S^+ [ionizations cm^{-3} s^{-1}] from [9] with x equivalent $\nu\beta p_{solid}\left(ew_{i,a}\right)^{-1}$. Equation 8 is valid for an applied voltage $V_s \gg kT_e$ between the electrodes and where the sheath dimension, s [cm] is less than the distance between electrode surfaces. Using the matrix sheath approximation

$$s = 10^{-1}\sqrt{\frac{2\varepsilon_0 V_s}{en_e}} \tag{9}$$

and by substitution of Equation 5 ($T_a = T_e$), s~1.1x10$^{-3}V_s^{1/2}{p_a}^{-1/4}$. For example, for applied voltages 2V≤ V_s ≤ 5V and power densities 10μW cm^{-3}≤ p_a ≤50μW cm^{-3} s ranges from (1.85 - 4.40)x10^{-2} cm.

Previous efforts [9] validated Equation 8, quantifying reactor power and gaseous composition effects on n_e and T_e. This work aims to illuminate electrode $\bar{A}$ effects on $\bar{I}_i$ and p_a. From Equation 8 for $V_s \gg kT_e$ and assuming the same source particle flux, microscopic cross section, and electrode volume, a voltage-independent ratio evolves between the foam and solid electrodes:

$$\frac{\left[\frac{\nu\beta}{m}\right]_f}{\left[\frac{\nu\beta}{m}\right]_s} = \left(\frac{I_{i,f}A_s}{I_{i,s}A_f}\right)^{4/3}\left(\frac{m_s}{m_f}\right)^2. \tag{10}$$

The electrodes' area and mass are readily measured as is the current drawn through them. $[\nu\beta/m]_f$ can be directly measured and compared to results obtained by modeling and simulation methods.

3. Experimental and M&S Approaches

To establish the proposed phenomena experimentally, I-V curves were measured on two electrode assemblies inserted into the neutron beam port cavity of a Mark II TRIGA nuclear reactor at the Nuclear

Engineering Teaching Laboratory at the University of Texas at Austin (Figure 2). For M&S validation, these assemblies were modeled in MCNP6.2, an industry-standard radiation transport code for electron and photon transport. The M&S results were compared to those from the experimental I-V curves.

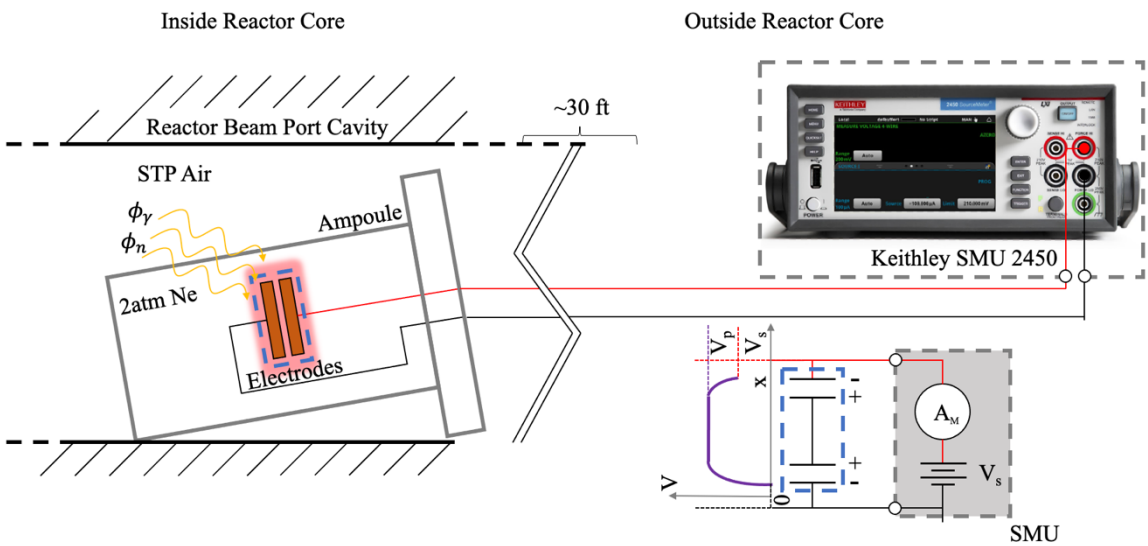

Figure 2. Experiment schematic and electrical circuit diagram (lower right hand corner). The electrodes float with respect to the plasma of constant density; this is modeled as two capacitors of opposite polarity connected in series through a lossless bulk plasma of potential V_p connected to voltage source V_s.

3.1. Experiment Description

The assemblies were designed and fabricated identically (besides the electrode assemblies), were both held under approximately 2atm neon and irradiated by the same neutron flux (thermal, epithermal, fast) (4.05, 2.06, 1.69)x10^{12} n cm^2 s^{-1} and gamma dose rate 1.99x10^{-2} W g^{-1} in Si. The electrodes consisted of 1) solid copper and 2) open-cell reticulated copper foam electrodes of approximately 60 pores per inch (ppi) and pore diameter ~5x10^{-2} cm. Additionally, one of the solid copper electrodes was coated with a thin layer (100nm) of dissimilar metal, molybdenum, to demonstrate the principle of converting the ion current into electrical power via electrodes of dissimilar work function. The thin layer contributes negligibly to the electrode's total mass and surface area and is assumed not to affect A_s or $\nu\beta$.

The reactor was operated at full power (950 kW) with the assemblies placed in the beam port cavity for 30 minutes before I-V measurements were taken to ensure the ^{66}Cu ($t_{1/2}$= 5.12min) had come into secular equilibrium; ^{64}Cu ($t_{1/2}$= 12.7hr), with its much longer half-life was not in secular equilibrium but varies negligibly over the I-V measurement time (around 3 minutes). The measurements were taken using a Keithley SMU 2450, which simultaneously sources user-defined voltages to and measures the corresponding current from the electrode assembly under test. Voltages were swept from -5V to 5V.

3.2. M&S Description

The complex structure of the open-cell reticulated copper foam was approximated by a cubic array of unit cells of length 470µm containing spherical pores of radius 250µm centered within the unit cell. The cell length and pore radius represent 60 pores per inch (ppi), 38% density electrode used in the experiment. A reflected boundary is used at the midplane of the interelectrode gap (1.5mm) to emulate a two-electrode system.

The energy deposition tally for electrons (F6:e) tracks the electron energy deposition in the solid and gaseous media per source particle, enabling a direct calculation of β. Source electrons originate from

the β^--decay of ^{64}Cu ($E_{\beta,ave}$ = 0.191MeV) and ^{66}Cu ($E_{\beta,ave}$ = 1.06MeV) upon thermal neutron capture and source photons from reactor generated gammas. The former is represented using a volumetric electron source within the electrode system and the latter with a volumetric photon source encapsulating the electrode system. Source particle energies from 0.1MeV to 2MeV in 0.1MeV increments were simulated.

4. Results

The I-V data is presented in Figure 2 where the solid electrode curve is shifted by the observed contact potential difference, $\phi_{Mo} - \phi_{Cu}$ of -0.25 eV – this demonstrates a power-producing ion current from the Mo to Cu electrode for V_s=0.0-0.25V, roughly 20 nW. Experimental $[\nu\beta/m]_f/[\nu\beta/m]_s$ data is presented in the left of Figure 3, where the "High A_f" and "Low A_f" scenarios account for the 15% uncertainty in the copper foams' surface areas. This range of $[\nu\beta/m]_f/[\nu\beta/m]_s$ overlays the energy- and source particle-dependent $[\nu\beta(E_0)/m]_f/[\nu\beta(E_0)/m]_s$ obtained by M&S in the right of Figure 3. From the left of Figure 3, a constant foam to solid electrode current ratio arises for 2V < V_s < 5V thereby satisfying the conditions $V_s \gg kT_e$ and s less than the smallest system dimension (i.e., the average pore diameter) for which Equations 8 and 10 are valid. Thus, a least squares regression in this applicable voltage range directly infers p_a according to Equations 4 and 8 where A is given by values in Table 3 and $\mu_{Ne_2^+}$ = 3.2 cm^2 V^{-1} s^{-1} [12]. p_a was determined to be (12.8-19.3) μW cm^{-3} and 70.1 μW cm^{-3} for the foam and solid electrodes, respectively. Directly substituting these values into Equation 6 gives corresponding n_e values (3.2-3.9)x10^9 cm^{-3} and 7.1 x10^9 cm^{-3}. For both electrodes $T_e \sim T_a$=300K.

Table 3. Electrode properties under irradiated conditions.

Electrode	m [g]	A [cm^2]	ν	β	p_{solid,β^-} [W cm^{-3}]	$p_{solid,\gamma}$ [W cm^{-3}]
Solid	16.88	13.49	27.5	8.3x10^{-6}	0.044	0.358
Foam	6.43	59±9	0.37	3.6x10^{-4}	0.017	0.136

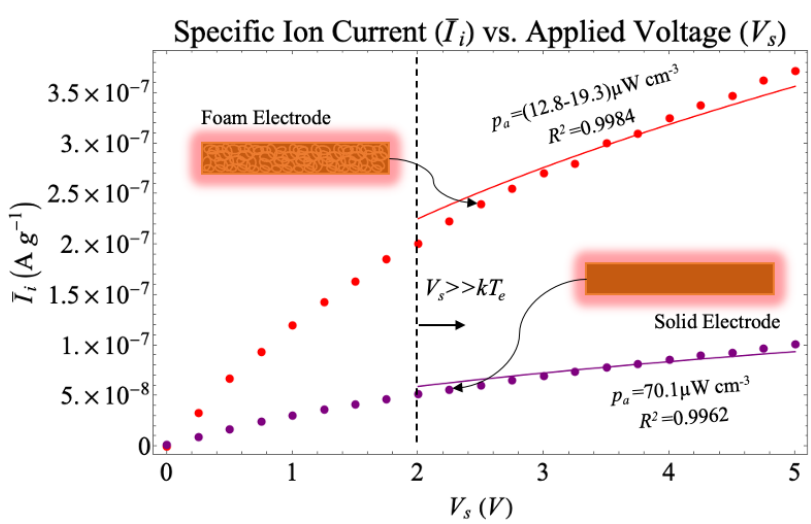

Figure 2. I-V curve for solid and foam copper electrodes. The corresponding curves (solid lines) are computed according to Equation 7. p_a is determined by a least squares regression for $V_s \geq$ 2V.

Interestingly, simulations predict an average $\nu\beta/m$ that is 50% higher for source electrons originating within the electrodes than for source photons originating outside the electrodes from 0.1-1.0 MeV and 25% higher from 1.0-2.0 MeV. However, this cannot be experimentally discerned due to the uncertainty in A_f. Future experiments, where A_f is more precisely known, could validate (or invalidate)

this M&S prediction. Despite this uncertainty in A_f for this initial experiment, the M&S and experimental results are in good agreement.

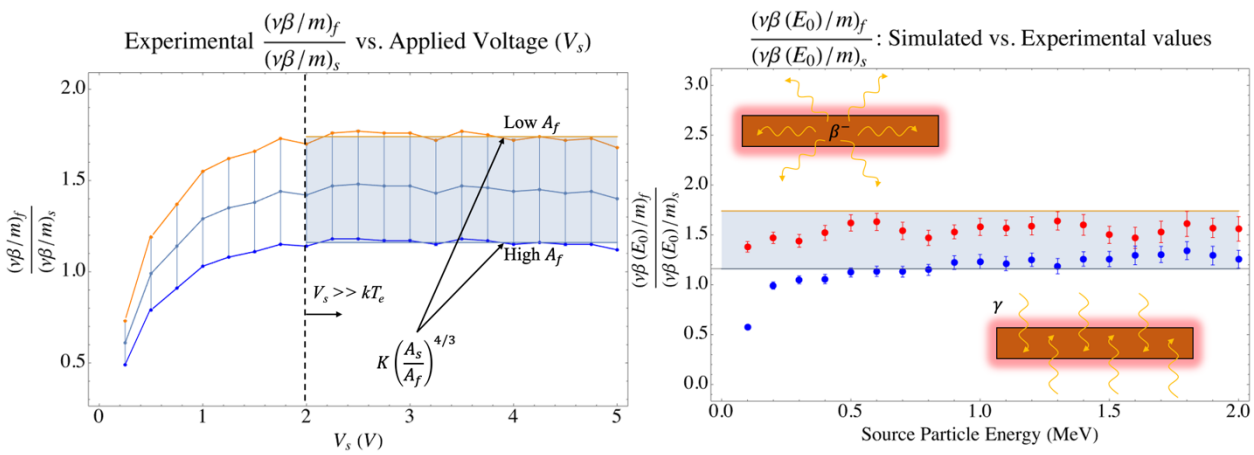

Figure 3. (Left) Experimental values for Equation 10 for high and low inferred values of $[\nu\beta/m]_f/[\nu\beta/m]_s$. $K = \left([m_s I_f]/[m_f I_s]\right)^{4/3}$) comprises values known to a sufficiently high precision so that they are not included in the error bar. (Right) MCNP simulation values for energy- and particle-dependent $[\nu\beta(E_0)/m]_f/[\nu\beta(E_0)/m]_s$ (photons = blue, electrons = red) compared to the average experimentally observed value (shaded blue).

4. Discussion

With the experimental and analytical methods now demonstrated, it is possible to extrapolate NLTP properties and pertinent scaling laws expected in porous media of a given solid and gaseous composition and electrode p_{solid}.

4.1. Scaling Laws

Equation 7 gives a direct relation between T_e and p_{solid}; n_e as a function of p_{solid} is obtained by tabulating $k_{dr}(T_e, T_a)$ values when solving Equation 7 then directly inserting these values into Equation 6. $n_e(p_{solid})$ and $T_e(p_{solid})$ are plotted in Figure 4 using $\nu\beta$ =1.4x10^{-4} n_a=5.0x10^{19} cm^{-3} and T_a=300K: representative values for this study's experimental conditions. We emphasize that this parameter space does not include the effects of using:

- Light and heavy ion-based NLTP ionization
- Penning gas mixtures
- Increased operating temperatures
- Diffusion-dominated density profile, where $n_e \propto p_{solid}$, for small pore dimensions

The first three would increase n_e or T_e (or both). Such effects (especially the last listed) should be investigated in future studies.

The specific ion and electron currents scale

$$\bar{I}_i \propto \bar{A}(p_{solid}\nu\beta)^{\frac{3}{4}}\mu_{a_2^+}^{\frac{1}{4}}$$
$$\bar{I}_e \propto \bar{A}\sqrt{\frac{p_{solid}\nu\beta T_e}{k_{dr}(T_e, T_a)}} \tag{11}$$

where $\bar{I}_i$ scaling follows from Equation 8 and $\bar{I}_e$ is assumed directly proportional to the random electron current $Aen_e\sqrt{\frac{kT_e}{2\pi m_e}}$. For example, when inserting values from Table 3 into Equation 11 to evaluate the foam-to-solid $\bar{I}_i$ ratio ($\bar{A}_{foam}$~55 cm^2 g^{-1}), one obtains the experimentally observed 3.5.

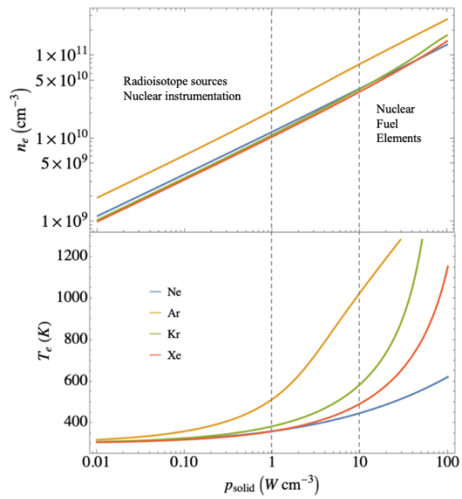

Figure 4. Expected plasma parameters $n_e(p_{solid})$ and $T_e(p_{solid})$ for porous media containing single species noble gases ionized by electrons assuming $\nu\beta$ =1.4x10^{-4} n_a=5.0x10^{19} cm^{-3} and T_a=300K.

For solid parallel plate (equal thickness) and coaxial[1] configurations:

$$\bar{A}_{par} \propto \frac{2}{\rho t}$$
$$\bar{A}_{ann} \propto \frac{2\left(1+\frac{r_2}{r_1}\right)}{\rho r_1} \tag{12}$$

where ρ [g cm^{-3}] is the solid density, t is the plate thickness [cm], and r_1 and r_2 [cm] are the inner radii of the inner and outer electrodes, respectively. For nuclear applications (e.g. neutron sensors) $\frac{r_2}{r_1}$ generally doesn't exceed 1.5. Assuming the characteristic pore dimension is much less than the total substrate dimension, the specific surface area for porous materials $\bar{A}_{por}$ is constant. Typical values for $\bar{A}_{por}$ for a 100ppi foam with 10% density material coating [13] are more than 1.5x10^2 cm^2 g^{-1}. For typical ρ values (5-10 g cm^{-3}), solid configurations must achieve t~(1-3)x10^{-3}cm and r_1~(3.5-7.0)x10^{-3}cm to attain similar values to $\bar{A}_{por}$. Even for the smallest commercially available fission chamber neutron sensors, r_1>5.0x10^{-2} cm [14]; for nuclear DEC systems such as the space nuclear reactor TOPAZ II, r_1>1cm [15].

The scaling laws above suggest that porous electrodes could enable significantly higher specific currents than traditional configurations. However, a better understanding of $\nu\beta$ scaling for various system conditions is necessary to determine porous electrodes' ultimate level of performance. Several factors including but not limited to electrode composition (solid and gaseous components), ionizing charged particle type, and $\bar{A}$ will all affect $\nu\beta$ appreciably; only continued experimental and M&S simulation efforts will begin elucidating this new design paradigm. Training, research, and test reactors are ideal testing facilities for NLTPs, able to generate wide power densities in various materials speedily and economically.

[1] The outer radius of the outer electrode is assumed to be negligibly larger than the inner radius, thus its volume contribution is neglected.

5. Conclusion

This work demonstrated an experimental and M&S basis for producing and analyzing NLTPs within complex electrode structures with $\bar{A}$ ~10 cm^2 g^{-1}. More optimized porous electrodes have the potential to facilitate dramatically higher specific power and current extraction in nuclear DECs and sensors. Such devices could use available manufacturing techniques to dispense the neutron-active or radioactive isotope itself within the porous structure, enabling the construction of large-scale systems (potentially m^3) [16]. Previously unexplored, NLTPs of this nature could have broad applications to energy systems, offering opportunities for cross-pollination between the nuclear and LTP science and engineering communities. Through continued interest and investigation into these NLTPs by a diverse research community, more uses will undoubtedly be discovered.

6. References

[1] C.B. Leffert, D.B. Rees, and F.E. Jamerson, "Investigations on the Direct Energy Conversion of Nuclear Fission Energy into Electrical Energy in a Plasma Diode," ONR Final Report, Contract Nonr-3190(00), February 1968.

[2] S.P. Melnikov, A. Sizov, A. Sinyanskii, and G.H. Miley, *Lasers with Nuclear Pumping*, Springer, 2015.

[3] Knoll, Glenn, *Radiation detection and measurement*, Wiley, 2010.

[4] G.H. Miley, "Overview of nuclear-pumped lasers," Laser and Particle Beams **11**, 575–581, 1993.

[5] A. Shapiyeva, E. Son, and S. Kunakov, "Formation of Energy Spectra of Electrons in a Dense Weakly Ionized Plasma Generated by Fission Fragments," Contributions to Plasma Physics **62**, January 2022.

[6] R.K. Bull, "Stopping powers for electrons and positrons: ICRU report 37," International Journal of Radiation Applications and Instrumentation. Part D. Nuclear Tracks and Radiation Measurements **11**, 1986.

[7] H.H. Andersen and J. F. Ziegler, *Hydrogen stopping powers and ranges in all elements, The Stopping and Ranges of Ions in Matter; Volume 3*, Pergamon Press, 1977.

[8] R.L. Platzman, "Total Ionization in Gases by High-Energy Particles: an Appraisal of our Understanding," International Journal of Applied Radiation and Isotopes **10**, 1961.

[9] C.B. Leffert, D.B. Rees, and F.E. Jamerson, "Noble Gas Plasma Produced by Fission Fragments," Journal of Applied Physics **133,** 1966.

[10] A.T. Lo, *Fission Plasmas and their Novel Application to Power Producing Nuclear Reactors in Space*, Ph.D. thesis, University of California, Berkeley, 2020

[11] G. A. Batyrbekov, Y. D. Kuznetsov, B. Y. Pel'menshtein, and Z. S. Takibaev, "Properties of the Inert Gas Plasma Formed by Uranium Fission Fragments in a Nuclear Reactor," Journal of Technical Physics **46**, 1976.

[12] L. Viehland and E. Mason, "Transport Properties of Gaseous Ions over a Wide Energy Range, IV," Atomic Data and Nuclear Data Tables **60**, 1995.

[13] Ultramet Advanced Material Solutions, "Open-cell Foam Tech Sheet," https://ultramet.com/wp-content/uploads/2017/10/Open-Foam-tech-sheet.pdf.

[14] D. Nichols, *Development and optimization of the micro-pocket fission detector* Ph.D. thesis, Kansas State University, 2022.

[15] M.S. El-Genk and H. Xue, "Transient and Steady-State Analyses of an Electrically Heated Topaz-II Thermionic Fuel Element," in 27th Intersociety Energy Conversion Engineering Conference, 1992.

[16] D. Youchison, R. Lenard, B. Williams, T. Stewart, and S. Anghaie, "A Tricarbide Foam Fuel Matrix for Nuclear Thermal Propulsion," in 42nd AIAA/ASME/SAE/ASEE Joint Propulsion Conference Exhibit, 2006.